ARTICLE

BIOTECHNOLOGY and BIOENGINEERING

Photonic Immobilization of BSA for Nanobiomedical Applications: Creation of High Density Microarrays and Superparamagnetic Bioconjugates

Antonietta Parracino,[1] Gnana Prakash Gajula,[1] Ane Kold di Gennaro,[1] Manuel Correia,[1] Maria Teresa Neves-Petersen,[2] Jens Rafaelsen,[1] Steffen B. Petersen[3,4]

[1]Department of Physics and Nanotechnology, Aalborg University, Skjernvej 4A, Aalborg, Denmark

[2]Nanobiotechnology Group, Department of Biotechnology, Chemistry and Environmental Sciences, Aalborg University, Sohngaardsholmsvej 49, Aalborg, Denmark

[3]Nanobiotechnology Group, Department of Health Science and Technology, Aalborg University, Frederik Bajers Vej 7D2, Aalborg, Denmark; telephone: +45-99408469; fax: 98154008; e-mail: sp@hst.aau.dk

[4]University at Buffalo, The State University of New York Buffalo, The Institute for Lasers, Photonics and Biophotonics, New York, New York

Received 30 June 2010; revision received 27 September 2010; accepted 1 November 2010

Published online 1 December 2010 in Wiley Online Library (wileyonlinelibrary.com). DOI 10.1002/bit.23015

ABSTRACT: Light assisted molecular immobilization has been used for the first time to engineer covalent bioconjugates of superparamagnetic nanoparticles and proteins. The technology involves disulfide bridge disruption upon UV excitation of nearby aromatic residues. The close spatial proximity of aromatic residues and disulfide bridges is a conserved structural feature in proteins. The created thiol groups bind thiol reactive surfaces leading to oriented covalent protein immobilization. We have immobilized a model carrier protein, bovine serum albumin, onto Fe_3O_4@Au core–shell nanoparticles as well as arrayed it onto optically flat thiol reactive surfaces. This new immobilization technology allows for ultra high dense packing of different bio-molecules on a surface, allowing the creation of multi-potent functionalized active new biosensor materials, biomarkers identification and the development of nanoparticles based novel drug delivery system.

Biotechnol. Bioeng. 2011;108: 999–1010.

KEYWORDS: superparamagnetic core–shell nanoparticles; LAMI light assisted protein immobilization; protein bioconjugates; biosensor arrays; drug carrier protein

Introduction

Advanced clinical diagnostic methods have been developed in order to understand the molecular mechanisms underlying disease processes. Since biomolecules such as nucleic acids and proteins are nanosized, probes of equivalent dimensions are very efficient tools at the subcellular level. New nanotechnological applications have recently emerged such as drug targeting and delivery (Huang and Lee, 2006), cell labeling and separation (Park et al., 2007), cancer therapy (Chu et al., 2006), magnetic resonance image (MRI) contrast agents (Cho et al., 2006), bio-sensors (You et al., 2007), and bio-imaging (Sharma et al., 2006). Among nanomaterials, magnetic core–shell nanoparticles resulting from the combination of metals with relevant optical, electrical, magnetic and catalytic properties can be used for nano applications. Fe_3O_4@Au particles are widely used because of their chemical stability, easy dispersibility, affinity towards biomolecules and convenient preparation techniques (Daniel and Astruc, 2004; Laurent et al., 2008). Their magnetism is used extensively in biosciences even for tissue engineering and to build complex 1D–3D structures (Ito et al., 2004; Lee and Liddell, 2009; Safarik and Safarikova, 2002). Tuning their plasmonic properties, by changing shell thickness, physic-chemical environment or through interactions with fluorophores, can greatly contribute to the development of clinical diagnosis

Antonietta Parracino and Gnana Prakash Gajula contributed equally to the work.

Correspondence to: S.B. Petersen

Contract grant sponsor: Fundação para Ciência e Tecnologia (FCT)

Contract grant number: SFRH/BD/61012/2009

methods (Baptista et al., 2008; Imahori et al., 2001; Lyon et al., 2004).

Since biomolecules are highly sensitive to pH, temperature and chemical environment, immobilization protocols should secure high molecular activity and stability. Incorporation of chiral molecules onto nanoparticles leads to specific protein surface recognition (You et al., 2008). Trypsin immobilization onto super-paramagnetic nanoparticles allowed using high enzyme concentrations leading to shorter digestion times, facilitating the separation of derivatized nanoparticles from solution (Li et al., 2007). Immobilization of biomolecules not only easies their separation and manipulation but also increases enzyme stability towards pH, temperature, chemical denaturants and organic solvents as well as preventing auto proteolysis (Yang et al., 2004, 2008). Several proteins have been coupled to magnetic particles using organic agents (Koneracka et al., 2002; Mehta et al., 1997) or by carrying out the reaction through ligand exchange, metal ions affinity, electrostatic as well as hydrophobic interactions (Brewer et al., 2005; Ma et al., 2006; Park et al., 2007). The covalent bond between thiol groups and gold surfaces is stronger than electrostatic interactions (Di Felice and Selloni, 2004; Uvdal et al., 1992; Varghese et al., 2008).

UV light assisted molecular immobilization (LAMI) is a novel photonic technology that results in covalent and uniform orientated coupling of biomolecules onto thiol reactive surfaces (Duroux et al., 2007; Jonkheijm et al., 2008; Petersen et al., 2006; Neves-Petersen et al., 2009a,b; Skoven et al., 2009a,b). The technology involves formation of free, reactive thiol groups upon UV excitation of protein aromatic residues located in spatial proximity of disulfide bridges, a conserved structural feature in proteins. LAMI has been successfully used to array functional biomolecules of medical interest (Duroux et al., 2007). LAMI combined with the Fourier-transforming properties of lenses as well as with a simple millimeter scale feature spatial mask lead to high-density protein arrays with a spatial resolution of a few hundred nanometers. An improvement of tenfold over existing commercially available high-density protein arraying methods was demonstrated (Neves-Petersen et al., 2009b; Skoven et al., 2009a).

In this paper we report light assisted immobilization of a carrier protein, BSA, onto Fe_3O_4@Au core–shell nanoparticles for the first time, as well as arrayed BSA onto a thiol reactive surface using LAMI. BSA has aromatic residues in close spatial proximity of disulfide bridges making it a good candidate for LAMI. Furthermore, we report the synthesis of Fe_3O_4@Au core–shell nanoparticles and the characterization of the engineered bioconjugates using spectroscopy techniques. In house imaging software package was used for advanced analysis of the protein array images and also to understand the nanoparticle size distribution. Binding therapeutic molecules onto nanoparticles leads to sensitive nanoprobes for bio-medical applications such as bio-separation, bio-sensing, drug delivery, and cellular specific binding.

Materials and Methods

Preparation of Fe_3O_4@Au Core–Shell Nanoparticles

Successive precipitation of two metals from metal precursors is used for the preparation of magnetic core–shell particles. Acidic solutions of 0.1 M $FeSO_4.7H_2O$ and 0.2 M $FeCl_3$ (pH 1) were mixed in 1:1 ratio upon constant stirring at room temperature. pH was rapidly increased to 10 by adding 10 mL 25% aqueous ammonia. Ten minutes after the solution turned black, 10 mL 1.0 M sodium citrate was added and the solution was stirred for 30 min. These magnetite particles were used as seeds onto which gold was deposited by citrate reduction method. One milliliter of the above suspension was transferred into 100 mL 1 mM sodium citrate. The solution was heated with constant stirring. Upon boiling, 10 mL 0.01 M $HAuCl_4$ solution was rapidly added and stirred for 30 min. The solution turned deep red, the characteristic color of gold colloids indicating presence of metallic gold. The suspension was cooled to room temperature and washed twice with water and centrifuged (10,000 rpm for 10 min) in order to eliminate excess surfactant and reaction byproduct salts. The supernatant was decanted. Bottom agglomerated particles were re-dispersed in water and re-washed.

Protein Labeling

BSA-AF532 labeling was carried out according to the protein labeling kit (A10236) from Molecular Probes (Invitrogen, Leek, The Netherlands). After labeling, BSA was dialyzed against 10 mM Tris–HCl buffer pH 7.5. Labeled protein concentration and degree of labeling (DOL) were calculated measuring the Abs^{530nm} using 81,000 $cm^{-1}\,M^{-1}$ as the molar extinction coefficient of AF532 at 530 nm. DOL was 1.46. 0.02 M ANS solution in dimethylsulfonic acid (DMSO) was diluted to 70 μM in 10 mM Tris–HCl pH 7.5 buffer. Concentration was calculated using 5,000 $cm^{-1}\,M^{-1}$ as the extinction coefficient of ANS at 350 nm. Protein–nanoparticle bioconjugates were incubated with an excess of ANS (1:10 molar ratio). ANS protein binding was monitored upon measuring the characteristic ANS absorption peak at 350 nm. Characteristic protein absorption was monitored at 220 and 280 nm.

Photonic Immobilization of BSA Onto Functionalized Slide

Chemical modification of optically flat quartz slides and optical setup used for immobilization were carried out as previously described (Duroux et al., 2007). One microliter of 7 μM BSA/AF532 was placed and dried on the thiol functionalized slide. A UV laser beam (1 mW, 280 nm) was sent through a computer controlled shutter, a beam expander and an iris diaphragm and focused through a quartz lens onto the sample mounted on a computer controlled 3D translation stage. One hundred milliseconds exposure time was used. A 4×6 array with 20 μm spots

interspaced 150 μm was created. The slide was washed with 1% Mucasol for 1 h changing the mucasol solution every 15 min and scanned with a Tecan LS 200 scanner for protein array visualization (exc. 532 nm, 6 μm resolution).

Photonic Immobilization of BSA Onto Gold Coated Superparamagnetic Nanoparticles

A sample containing 8.0 μM BSA and 0.8 μM concentration of gold in the form of nanoparticles superparamagnetic nanoparticles in 10 mM Tris–HCl buffer pH 7.5 was illuminated for 1 h with 295 nm light in a RTC 2000 PTI spectrofluorimeter. Lamp power at the sample location was 142 nW. Slits were kept at 5 nm and temperature at 20°C. The sample was stirred every 10th minute during illumination. The uncoupled BSA was washed out by two centrifugations and particle-protein bioconjugates were re-dispersed in buffer and characterized. As a negative control, identical experiments were carried out in the absence of UV illumination.

UV–Visible Absorption Spectroscopy

Thermo scientific UV–visible spectrophotometer (VWK International UV1 v4.60, West Chester, PA) was used to characterize the free thiol groups in BSA, nanoparticles, protein, degree of labeling and protein coated nanoparticles. The path length of the quartz cuvette was 1 cm. Absorbance spectra were acquired between 220 and 700 nm.

Ellman's Reactions

Ellman's assay was used to determine the concentration of free thiol groups in BSA prior to and after 1 h 295 nm excitation upon measuring the intensity of the absorption at 412 nm (Riener et al., 2002). BSA concentration was 8.0 μM in 10 mM Tris–HCl buffer pH 7.5. Ellman's reagent (5,5′-dithiobis(2-nitrobenzoate), DTNB) concentration was 500 μM.

Fluorescence Spectroscopy

Fluorescence characterization of native BSA, BSA-AF532, and BSA-ANS coupled to nanoparticles were carried out in a RTC 2000 PTI spectrofluorimeter at 20°C. Quartz cuvette path length was 1 cm. Slits were set at 5 nm. Intrinsic protein fluorescence spectra were acquired upon 295 nm excitation. Extrinsic fluorescence emission spectra of BSA-AF532 were acquired upon 530 nm excitation. Intrinsic protein fluorescence spectra were acquired upon 295 nm excitation. ANS fluorescence spectra of BSA-ANS alone and coupled to nanoparticles were acquired upon 350 nm excitation.

Dynamic Light Scattering (DLS)

Measurements were carried out in a Zsizer Malvern with temperature controlled MicroSampler. Average hydrodynamic size and size distribution of the core–shell nanoparticles, protein, and protein tagged nanoparticles were estimated. Fifty microliters was transferred to a 1 cm path length cuvette for each measurement.

Scanning Electron Microscopy—Energy Dispersive X-Ray spectroscopy (SEM-EDS)

Carl Zeiss 1540XB SEM with Noran EDS system was used for particle's size estimation and composition. SEM images were collected upon optimizing the voltage between 5 and 12 kV on silicon substrate where dried magnetic core–shell particles were placed. The average size of core–shell nanoparticles and protein–particles bioconjugates were estimated. The electron beam was focused over the particle projection area during X-ray acquisition. The X-ray spectrum was acquired for 60 s, at an acceleration voltage of 12 kV. NORAN system six version 2.0 software from Thermo Fischer scientific was used to analyze the EDS data (particles' chemical composition).

Fluorescence Microscopy

Nanoparticles coupled to labeled proteins were visualized with a fluorescence microscope (Leica TCS SP5) in oil-immersion 60× objective and images recorded with CCD camera. Before imaging, the samples were dried over the glass slide surface at room temperature. In order to image AF532, N2.1 filter cube was used (exc 515–560 nm; long pass filter (LP) at 590 nm). For ANS, A4 filter cube was used (exc 340–380; LP 425 nm).

Particles and Protein Array Image Processing

MATLAB v7.8 was used to develop BNIP-Pro software package that allows for advanced image analysis. The SEM image was baseline corrected using manually placed multiple control points in the base of the image. The image was then converted to a binary image, using a threshold value that allowed for the observation of a maximum number of separated particles. Morphological erosion and dilation was applied to the binary image in order to break residual contacts between particles. The modified binary image was then multiplied with the original image, leading to an image where only the particles are visible. Contours were draw around all particles, and their individual area and intensity analyzed.

Pairwise Sequence Alignment

Clustal W, version 2, was used to carried out the pairwise sequence alignment of BSA (607 aa) and HSA (585 aa). The matrix used was EBLOSUM62 with gap penalty 10 and extended penalty 0.5.

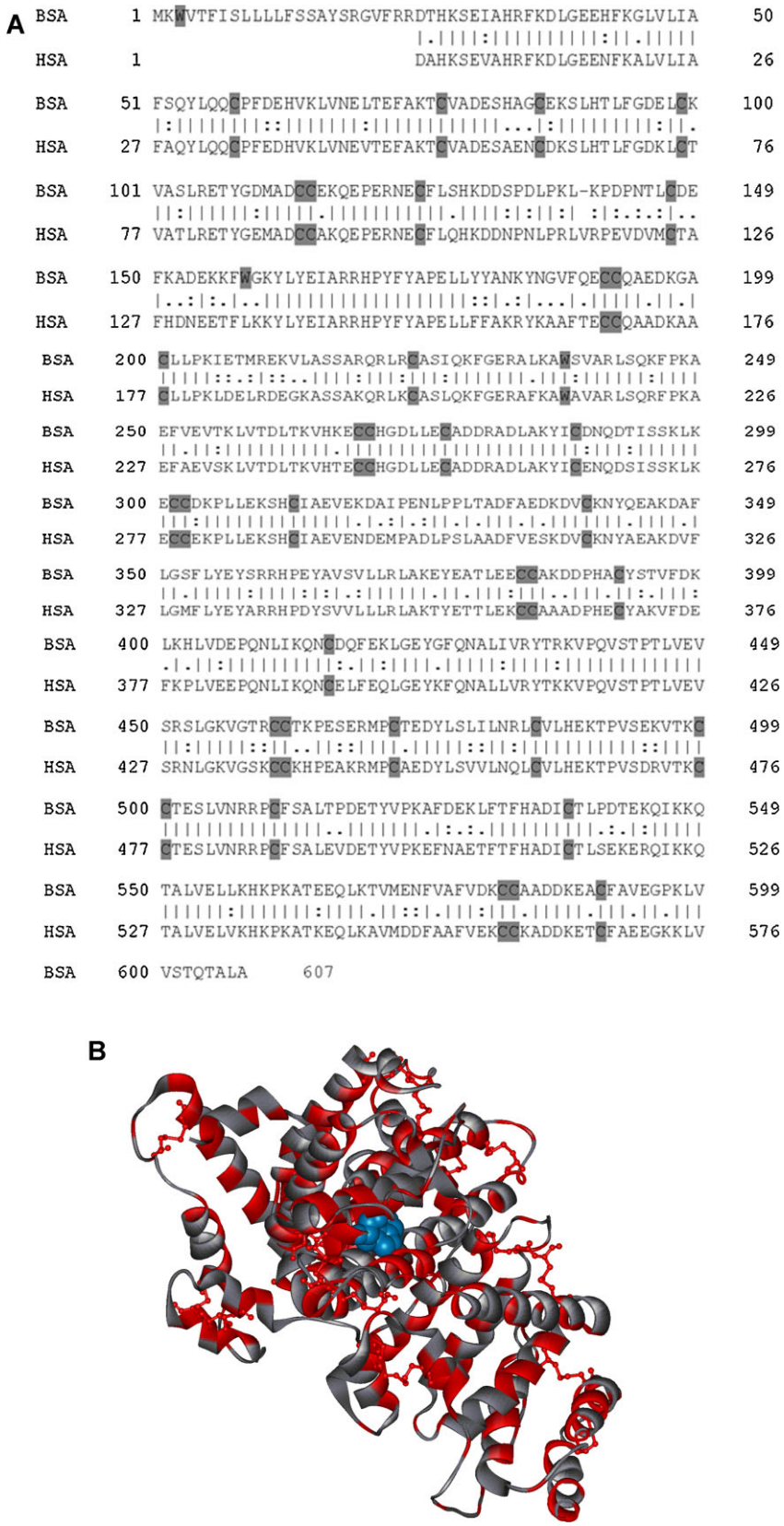

Figure 1. **A**: Pairwise sequence alignment of BSA and HSA. Standard one letter abbreviations are used for the amino acids; (|) Indicates identical amino acids; indicates similar (homologous) amino acids; (:) indicates unrelated amino acids. The cysteins (C) and tryptophans (W) are highlighted in gray and bold. Moreover, all 35 cysteins are conserved. **B**: 3D representation of HSA (PDB code: 1ao6) which displays identity, similarity, and gap of 72.6%, 84.2%, and 4.3%, respectively with BSA [http://www.ebi.ac.uk/Tools/emboss/align/]. Cysteines are highlighted in red ball and stick; W 214 is highlighted in blue CPK and the hydrophobic amino acids are highlighted in red.

Results and Discussion

Protein Characterization

Since BSA 3D structure is not available, a pairwise sequence alignment between BSA and human serum albumin (HSA) has been carried out, revealing identity, similarity and gap of 72.6%, 84.2%, and 4.3%, respectively. Alignment not only shows high identity between the two proteins but also reveals a consistently dispersed identity and similarity (Fig. 1A). Thus, structural homology can be inferred. It is likely that the distances between homologous Trp and disulfide bridges in HSA may be comparable to those in BSA. The shortest distance between conserved Trp214 chainA and the nearest disulfide bridge (Cys200–Cys246) in HSA is 11 Å. The 3D structure of HSA is shown in Figure 1B. HSA contains 1 tryptophan and 17 disulfide bridges. BSA contains 3 Trp residues and 17 disulfide bridges and one free thiol group Cys34. Cys34 has low or no solvent accessibility making it difficult to react with the nanoparticles' Au surface (Brahma et al., 2005; Wang et al., 2009; Zhu et al., 2001). The combined presence of 3 Trp and 17 disulfide bridges make BSA a good candidate for LAMI technology.

Thiol Groups Formation Upon 295 nm Irradiation

UV-light induced changes in amino acid residues of proteins have been reported (Bent and Hayon, 1975a,b; Creed, 1984a,b,c Kerwin and Remmele, 2007; Grossweiner and Usui, 1971; Li et al., 1989; Neves-Petersen et al., 2009b). Tryptophan (Trp) has the highest absorption coefficient in the near UV region. Since excitation has been carried out at 295 nm, we will focus on Trp photochemistry. Flash photolysis studies of lysozyme demonstrated that enzyme inactivation was due to the production of photo-oxidized tryptophan residue and due to electron transfer between Trp triplet state and a nearby disulfide bridges, resulting in SS disruption. Two non-radiative relaxation pathways were observed: (1) Electron ejection to the solvent, yielding solvated electrons e^-_{aq} ($Trp + h\nu \rightarrow Trp^{\bullet +} + e^-_{aq}$), (2) Intersystem crossing, yielding the triplet-state ^3Trp ($^1Trp + h\nu \rightarrow {}^1Trp^* \rightarrow {}^3Trp$). e^-_{aq} and ^3Trp can transfer an electron to a nearby disulfide bridge forming $RSSR^{\bullet -}$, which will lead to SS disruption (Sander et al., 1993):

$$RSSR^{\bullet -} \Leftrightarrow RS^{\bullet} + RS^-$$
$$RSSR^{\bullet -} + H^+ \Leftrightarrow RS^{\bullet} + RSH$$
$$H^{\bullet} + RSSR \rightarrow RS^{\bullet} + RSH$$

The resultant free thiol radicals/groups can then form a new disulfide bridge with other thiol groups or thiol reactive surfaces. This can be used to carry out LAMI of proteins onto thiol reactive surfaces. Therefore, LAMI is used to immobilize BSA onto thiol derivatized slides as well as superparamagnetic particles aiming at the development of nanoparticles based drug delivery system and biosensors. Our earlier work as well as Vanhooren's work verified the crucial role of Trp on the photolytic cleavage of disulfide bridge using protein engineering (Petersen et al., 2006; Vanhooren et al., 2006). The estimated concentration of free thiols in BSA before and after 1 h 295 nm illumination was 0.35 and 0.98 μM, respectively. The value for non-illuminated sample is due to the presence of Cys34 (though it is difficult to bind with Au surface, it can react with some probes (Brahma et al., 2005; Wang et al., 2009; Zhu et al., 2001)) and the observed increase in free thiol groups concentration after excitation indicates disulfide bridge disruption upon 295 nm excitation.

For LAMI we use energy per pulse $\leq$100 pJ, which is at least 10^7 times smaller than the energies required in the flash photolysis studies. No protein denaturation has been observed while carrying out the hereby presented illumination experiments. Circular dichroism, dynamic light scattering, steady state fluorescence and static light scattering experiments indicate that 295 nm excitation (excitation carried out at the spectrofluorimeter) did not induced structural changes, for example, denaturation and aggregation of BSA (data not shown).

Microarray Visualization

A 4 × 6 BSA array with 20 μm diameter spots and 150 μm pitch is displayed in Figure 2. BSA-AF532 extrinsic fluorescence can be observed. The spots are well resolved indicating that protein has been washed out from regions of the slide that have not been illuminated. The array shows uniform vertical and horizontal fluorescence intensity profiles (Fig. 2).

Fe_3O_4@Au Core–Shell Nanoparticles Characterization

Citrate stabilized magnetite nanoparticles dispersion is shown in Figure 3A (brown color dispersion, I). Magnetite nanoparticles were nucleated by simultaneous reaction of iron salts hydrolysis into Fe^{2+}-Ferrihydrite complex material (at pH < 8) and condensation of the complex into inverse spinel structure (pH > 8) (Tronc et al., 1992). Particles below critical size (~26 nm for magnetite) exhibit superparamagnetism where the coercivity and remenence of the hysteresis loop are zero. These particles can therefore be controlled by external magnetic fields but retain no residual magnetism after the field is removed since thermal energy overcomes the anisotropic energy barrier.

While preparing magnetic core–shell particles, citric acid plays four major roles: (1) Prevention of magnetite nanoparticles agglomeration immediately after nucleation due to affinity between carboxylic group and iron oxides (Lesnikovich et al., 1990), (2) Reduction of gold cations (Au^{3+}) into gold (Au^0), (3) Stabilization of Fe_3O_4@Au core–shell nanoparticles (magnetic nanoparticles were very stable with zeta potential of −75 mV at pH 9 (Lattuada and Hatton, 2007)), and (4) Easy replacement of citrate ions on the gold surface by thiol groups. Gold cation in the form

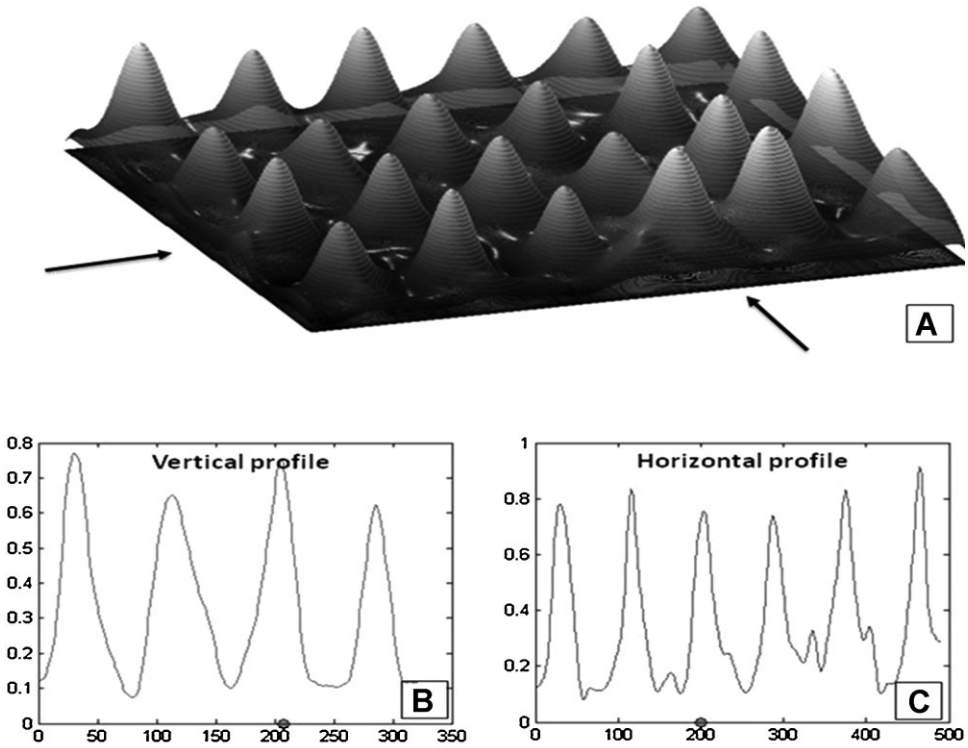

Figure 2. Microarray of BSA-Alexa-Fluor532 immobilized onto the SH functionalized optical flat surface through LAMI technique (**A**). The array contains 4 × 6 spots with 150 μm pitch and each spot is ~20 μm in diameter. Uniform vertical and horizontal fluorescence emission intensity profiles are displayed in **panels B and C**, respectively.

$AuCl_4^-$ is a strong oxidizing agent with $E^0 + 1.002$ (Cushing et al., 2004). Therefore, biocompatible weaker reducing agents such as carboxylates or alcohols can be used to reduce these cations. Since citrate ions are weak reducing agents, gold salt reduction process occurs at a slow reaction rate and precipitation onto existing seed magnetite particles is observed instead of primary nucleation. The use of borohydride as well as other strong reducing agents results in the formation of a large number of tiny gold particles due to high reaction rate (Gnanaprakash et al., 2007). In contrast, citrate reduction methodology leads to secondary nucleation on the magnetite core particles, resulting in the formation of Fe_3O_4@Au core–shell nanoparticles (Fig. 3A and II). The magnetic nature of the gold coated magnetite nanoparticles is shown in Figure 3A and III using a permanent magnet. Upon exposure to a permanent magnetic field, the wine-red (purple on dilution) color disappears leaving a clear solution behind and accumulating particles at the permanent magnet location (Fig. 3A and III). Upon magnetic field removal, the particles re-dispersed in solution.

Figure 3B displayed the SEM image of Fe_3O_4@Au core–shell nanoparticles. EDS experimental analysis qualitatively confirms the presence of the elements C, O, Fe, Na, Si, Au, and Cl (Fig. 3C). C, O, and Na peaks can be expected from sodium citrate surfactant; Si from substrate; Cl from buffer; Fe, Au, and O from Fe_3O_4@Au core–shell nanoparticles. The estimated average nanoparticle size observed with SEM was 22 nm. Using BNIP image analysis, the particles' size distribution was estimated (Fig. 3D). DLS measurements revealed an average hydrodynamic diameter (D_h) of 37.4 nm. The observed single peak confirmed that the particles dispersed in solution were isolated and not agglomerated (data not shown). The average size difference between the SEM and DLS measurements is due to the particles solvation by water and surfactant molecules in solution.

Absorption at 534 nm confirmed the presence of gold layer over the magnetite particles (Fig. 3E). Figure 3E displays the UV–visible absorption spectra of citrate stabilized particles of Fe_3O_4 (average size of 8 nm), Au nanoparticles (average size of 22 nm) and Fe_3O_4@Au nanoparticles (average size of 22 nm) in aqueous solution and of water (blank). Fe_3O_4 nanoparticles dispersion shows absorption band with maximum at 220 nm which extends into the visible region due to the charge transfer transitions involving Fe^{3+}–O and Fe^{2+}–Fe^{3+}(Schwertmann and Cornell, 1991). Plasmonic excitation of citrate stabilized 20 nm gold nanoparticles has a maximum at ~520 nm in agreement with literature (Brown et al., 2000). Fe_3O_4@Au particles show a clear surface plasmon absorption band at 534 nm (14 nm red shift compared to Au nanoparticles) and the suppression of the intense magnetite absorption peak in the UV region. Earlier works report similar shifts for gold

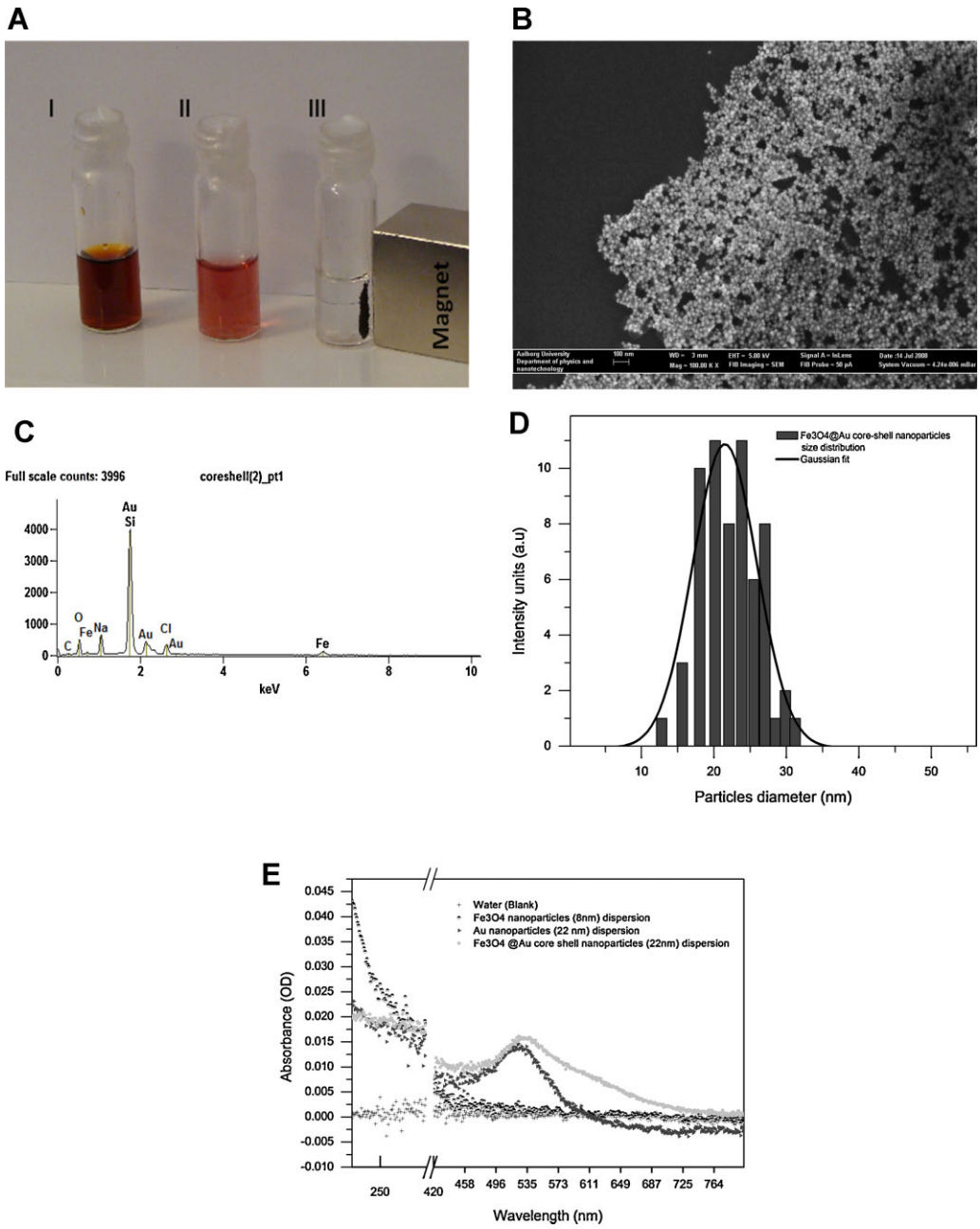

Figure 3. **A**: Display of samples containing (**I**) Magnetite dispersion (brown), (**II**) gold modified magnetite nanoparticles dispersion (purple) and (**III**) separation of superparamagnetic gold coated magnetite nanoparticles from solution using a permanent magnet, illustrating the separation potential of the technique. **B**: SEM image of Fe_3O_4@Au core–shell nanoparticles. The estimated average particle size is 22 nm. **C**: EDS analysis of gold covered superparamagnetic nanoparticles. **D**: Particles' size distribution obtained from BNIP image analysis. **E**: UV–visible absorption spectra of citrate stabilized particles of Fe_3O_4 (8 nm average size), Au nanoparticles (22 nm average size) and Fe_3O_4@Au nanoparticles (22 nm average size) in aqueous solution and of water (blank).

coated magnetite nanoparticles (Lyon et al., 2004; Wang et al., 2005). These previous studies revealed that the surface plasmon resonance property of the Au shell is dependent on its thickness. As the thickness of the gold layer increases the plasmon resonance peak gradually blue shifts towards 520 nm. The observed red shift (~14 nm) in the plasmon resonance peak, the suppression of magnetite absorption band in UV region for Fe_3O_4@Au nanoparticles (Fig. 3E) and the magnetic nature of the wine-red colored solution confirms the completely covered magnetite core with thick Au shell (more than 1 nm (Wang et al., 2005)).

At pH 7.5, gold covered magnetite nanoparticles (22 nm) are more stable than magnetite particles (8 nm) in solution. This is expected due to higher surface to volume ratio and magnetic dipole–dipole interactions in 8 nm magnetite dispersion than in 22 nm core–shell nanoparticles dispersion

(Lyon et al., 2004). Hence, depositing Au layer over magnetite particles is a better choice as compared to magnetite alone for the protein immobilization onto superparamagnetic nanoparticles.

Confirming BSA Immobilization Onto the Superparamagnetic Nanoparticles

At pH 7.5 the created free thiol groups will likely be partially deprotonated (typical pK_a in proteins from 8 to 11 (Creighton, 1993)), thus being more reactive towards gold. Since thiols bind stronger to gold than citrate does, citrate ions are usually substituted by thiols (Lim et al., 2008; Schmid and Corain, 2003). Therefore, Au–S bond is a likely bond between the protein and the core–shell nanoparticles. BSA and citrate stabilized gold nanoparticles interact electrostatically through carboxylate–ammonium salt bridges between the citrate and amino group of lysine and arginine on the protein surface (Brewer et al., 2005). Since the pI of BSA is 5.82, at pH 7.5 the protein will have a negative net charge. Therefore, it is likely that the protein molecules will replace citrate molecules and interact electrostatically with the positively charge Au surface. However, salt bridges interactions (2–15 Kcal/mol) are weaker than Au–S bonds (47 Kcal/mol). Thus, solvent accessible free thiol groups created in BSA are likely covalently bound to the gold nanoparticles surface. Thiol groups covalently bind gold surfaces through the sulfur atom (Bain et al., 1989; Uvdal et al., 1992). The reaction formally is considered an oxidative addition of the S–H bond to the gold surface, followed by reductive elimination of the hydrogen (Ullman, 1996; Varghese et al., 2008):

$$\text{R-S-H} + \text{Au}_n^0 \rightarrow \text{R-S}^-\text{Au}^+\text{Au}_\text{n}^0 + \frac{1}{2}\text{H}_2$$

Templeton et al. (1999) demonstrated that it is easy to replace one molecule with another present in higher concentration while providing enough heat and/or sonication. In order to optimize protein immobilization, protein concentration was kept 10-fold higher than the particles concentration. This will favor protein immobilization. Likewise the protein concentration should be higher than the citrate concentration. Finally, pH was adjusted to pH 7.5 in order to secure a significant proportion of deprotonated thiol groups and protein stability.

Binding of BSA onto the superparamagnetic nanoparticles was confirmed by DLS, SEM, UV–visible spectroscopy and fluorescent spectroscopy. Fluorescence emission spectra of the supernatant were acquired in order to monitor the removal of excess unbound protein from the nanoparticles after each washing step (Fig. 4A and B). Washing for a second time the derivatized nanoparticles lead to the removal of the majority of the unbound protein molecules. The intensity of the protein peak observed in the second wash was much smaller than the protein absorption peak of bottom settled particles, though the particles were diluted

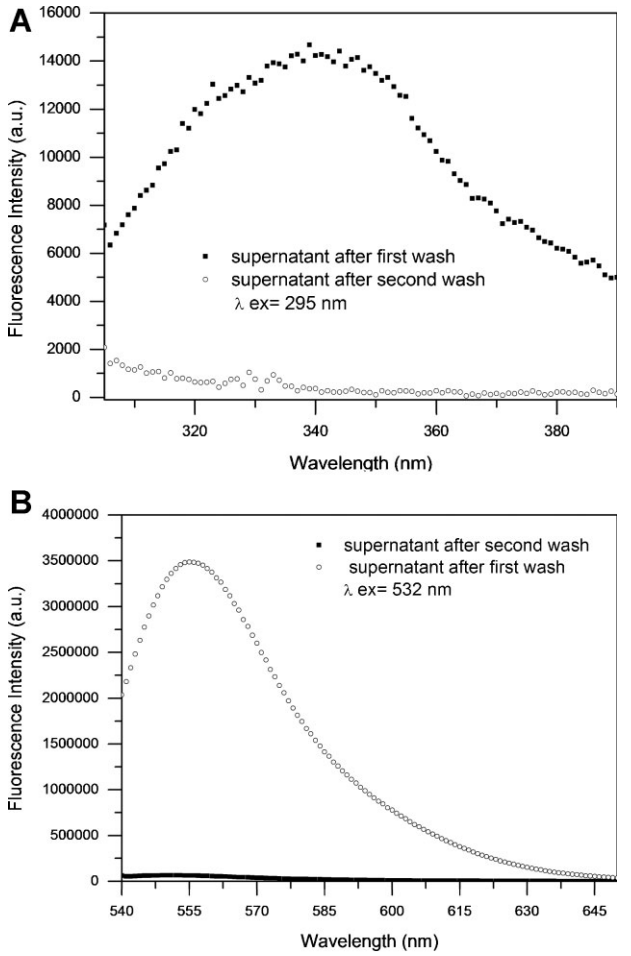

Figure 4. **A**: Fluorescence emission spectra of the supernatant recovered after the first and second washes. The proteins' intrinsic fluorescence was acquired upon 295 nm excitation. The spectra show the negligible amount of free protein present in the supernatant after the second wash. **B**: Fluorescence emission spectra of the supernatant recovered after the first and second washes. The proteins' extrinsic fluorescence was acquired upon 532 nm excitation. The spectra show the negligible amount of free protein present in the supernatant after the second wash.

500 times with buffer. Further washing did not show any significant change in the intensity of the protein absorption peak of the nanoparticle-BSA bioconjugates and of the supernatant. Data confirms that two washes were sufficient to remove non-immobilized protein from the solution (Fig. 4A and B). After two washing procedures, the bottom settled particles were re-dispersed in buffer and used characterized. BSA shows a hydrodynamic diameter (D_h) of 9.6 nm. The observed D_h values for the protein–particles bioconjugate showed a distinct dominant peak at 217 ± 63 nm in DLS, accounting for 95.5% of the signal. A smaller peak accounting for 3.3% of the signal has been observed centered at $1{,}029 \pm 309$ nm and a very small third peak centered at 5227 nm accounting for 1.2% of the signal (Fig. 5A). The polydispersity and the increase of the particles size indicates that aggregation of derivatized nanoparticles

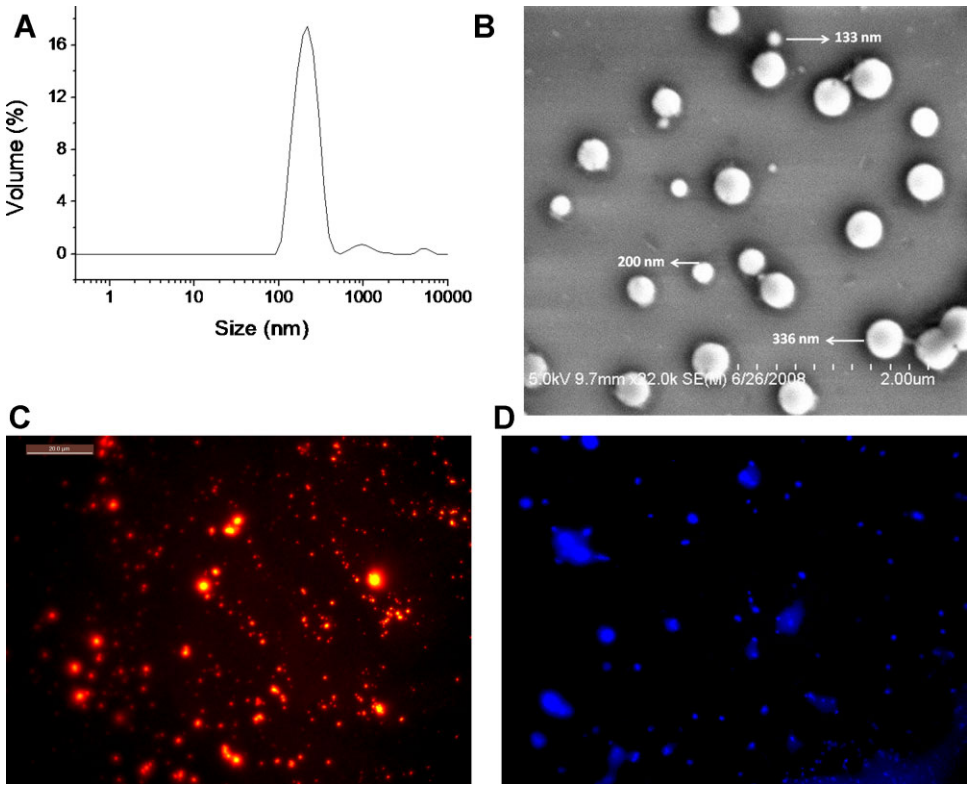

Figure 5. **A**: DLS data of BSA immobilized onto Fe_3O_4@Au core–shell nanoparticles showing a dominant peak at 217 ± 63 nm (95.5% volume). **B**: SEM image of BSA immobilized core–shell nanoparticles and observed sizes. **C**: Fluorescence microscopy images of BSA-AF532 immobilized onto Fe_3O_4@Au core–shell nanoparticles. **D**: ANS fluorescence from ANS molecules bound to BSA-Fe_3O_4@Au core–shell nanoparticles bioconjugates. ANS becomes fluorescent upon binding hydrophobic regions of BSA.

has occurred after protein immobilization. The protein derivatized nanoparticles were stable in solution and the particles–protein bioconjugate does not show any peak at 9.6 nm or 37.4 nm corresponding to free BSA or core–shell nanoparticles, respectively. When carefully observing the SEM data (Fig. 5B) we see bioconjugates at ~133, ~200, ~336 nm. All these peaks are located within the observed statistically relevant DLS peak at $\sim 217 \pm 63$ nm. The presence of 17 disulfide bridges in BSA makes it likely that upon UV excitation several bridges break, generating multiple free thiol groups. The reactivity of these groups induces aggregation among derivatized nanoparticles due to new SS bridges formed between several bioconjugates. Figure 5C displays the fluorescence of BSA-AF532 coupled to superparamagnetic gold coated nanoparticles, confirming the presence of labeled BSA onto the nanoparticles. In order to confirm protein immobilization onto the nanoparticles, ANS has been added to the derivatized nanoparticles. ANS is non-fluorescent in water and becomes fluorescent upon adsorption onto hydrophobic regions of the protein (Haugland, 2002). Figure 5D shows the fluorescence of the adsorbed ANS to the proteins bound onto the nanoparticles, confirming the presence of protein onto the core–shell nanoparticles.

Figure 6A displays the normalized fluorescence emission spectra of free (not immobilized) and immobilized protein, revealing a 15 nm blue shift in the fluorescence emission maximum after protein immobilization. A blue shift (~10 nm) in ANS fluorescence emission is also observed for Fe_3O_4@Au-BSA-ANS versus BSA-ANS (Fig. 6B). The blue shift is likely to be caused by the lower dielectric constant of the core–shell particles compared to the aqueous environment. Data confirms that ANS as well as the Trp becomes less solvent accessible upon BSA immobilization onto nanoparticles.

Figure 7A shows the UV–visible absorption spectra of nanoparticles with and without BSA-AF532. Core–shell particles show the single characteristic 534 nm gold absorption peak. The spectrum of functionalized nanoparticles shows characteristic protein absorption at 220 and 280 nm, and an enhanced peak at 530 nm. The peak at 280 nm is due to aromatic residues absorption, the peak around 220 nm is due to protein backbone absorption and the enhanced peak at 530 nm is due to the presence of gold and dye molecules attached to the protein. This clearly indicates the immobilization of protein onto the particles. The concentration of BSA tagged to nanoparticles was estimated to be 0.566 μM. The final molar ratio of coupled

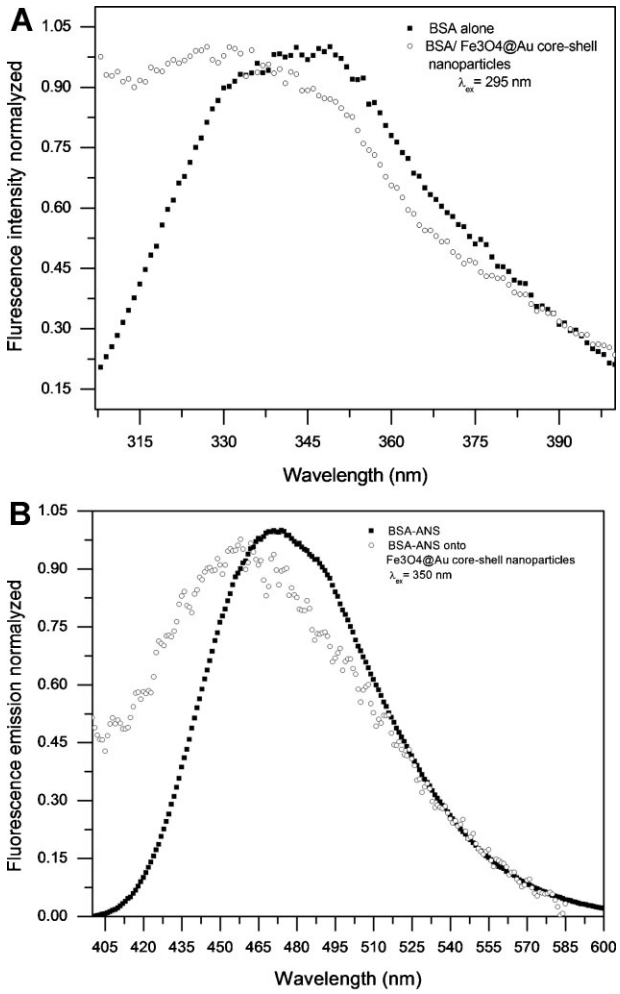

Figure 6. **A**: Normalized intrinsic fluorescence emission spectra of free BSA (not immobilized) and immobilized labeled BSA onto Fe_3O_4@Au core–shell nanoparticles. **B**: Normalized emission spectra of ANS bound to free BSA and ANS bound to BSA immobilized onto Fe_3O_4@Au core–shell nanoparticles. Spectra show a blue shift in the ANS fluorescence emission maximum when ANS is bound to the immobilized protein.

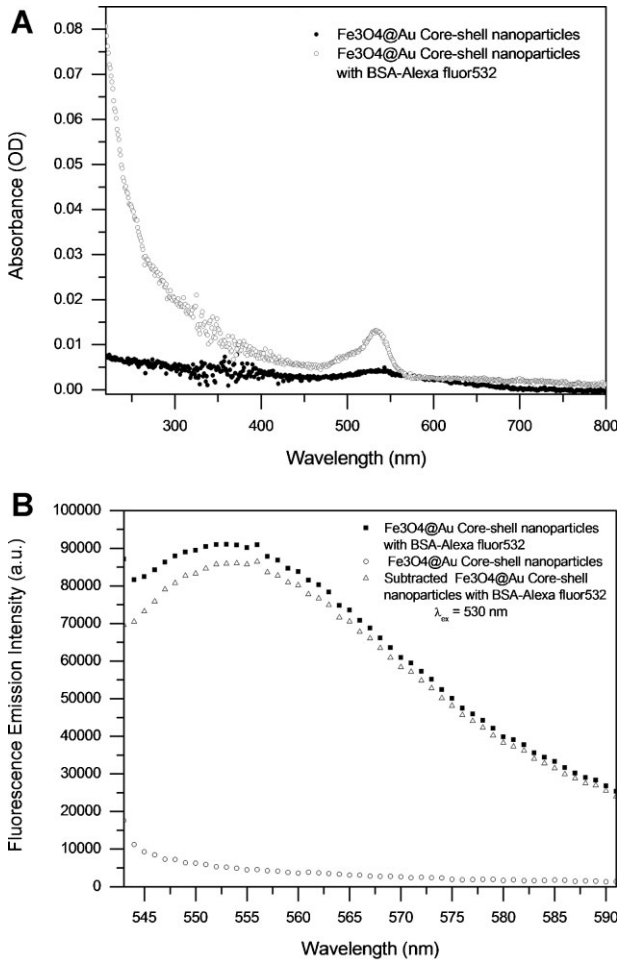

Figure 7. **A**: Absorption spectra of Fe_3O_4@Au core–shell nanoparticles with and without BSA-AF532. **B**: Fluorescence emission spectra of BSA-AF532 coupled Fe_3O_4@Au core–shell nanoparticles and of Fe3O4@Au core–shell nanoparticles. The difference spectrum is also displayed.

BSA-nanoparticles was 1:0.7 in solution indicating the successful immobilization of BSA onto Fe_3O_4@Au core–shell nanoparticles using LAMI. In Figure 7B it can be seen that nanoparticles alone do not show any significant fluorescence emission at 552 nm. However, when exciting BSA immobilized onto nanoparticles with 532 nm light a fluorescence emission peak is observed at 552 nm, confirming the presence of BSA on the nanoparticles' gold surface. The spectra obtained for the samples that were illuminated with UV light and for the non-illuminated samples (negative control) are displayed in Figure 8. The illuminated sample exhibits higher 552 nm fluorescence emission upon 532 nm excitation, while the non-illuminated sample shows low 552 nm fluorescence intensity, indicating that UV excitation has increased the immobilization yield of labeled protein onto the particles.

Conclusions

Immobilization of BSA on the surface of gold coated magnetite nanoparticles as well as on flat sensor surface has been achieved with LAMI. The protein–nanoparticles bioconjugates are more stable in solution than non-derivatised nanoparticles since it was always possible to re-disperse them into solution after centrifugation. The non-derivatised nanoparticles aggregated as a black pellet after two centrifugation/washing steps and no longer re-disperse. The photonic immobilization technology can lead to the creation of multi-potent covalently bio-functionalized new materials as well as drug and gene carriers. These results encourage future development of magnetic nanoparticle based protein carriers with targeted technological applications such as bioseparation, drug targeting, tissue engineering and to improve the enzyme stability towards pH, temperature and solvents.

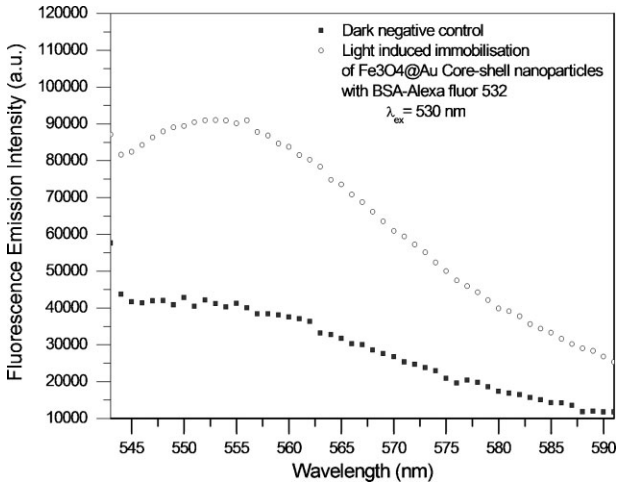

Figure 8. Fluorescence emission spectra of coupled Fe_3O_4@Au core–shell nanoparticles with BSAAF532 with and without light (negative control).

M.C. acknowledges the support from "Fundação para a Ciência e Tecnologia" (FCT) for the PhD grant (SFRH/BD/61012/2009) supported by "Programa Operacional Potencial Humano" (POPH) in the framework of "Quadro de Referência Estratégico Nacional" (QREN) and co-financed by the European Social Fund ("Fundo Social Europeu", FSE). G.P.G. acknowledges the support from the Danish National Advanced Technology Foundation (contract 010-2006-1).

References

Bain CD, Troughton EB, Tao YT, Evall J, Whitesides GM, Nuzzo RG. 1989. Formation of monolayer films by the spontaneous assembly of organic thiols from solution onto gold. J Am Chem Soc 111:321–335.

Baptista P, Pereira E, Eaton P, Doria G, Miranda A, Gomes I, Quaresma P, Franco R. 2008. Gold nanoparticles for the development of clinical diagnosis methods. Anal Bioanal Chem 391:943–950.

Bent DV, Hayon E. 1975a. Excited state chemistry of aromatic amino acids and related peptides. III. Tryptophan. J Am Chem Soc 97:2612–2619.

Bent DV, Hayon E. 1975b. Excited-state chemistry of aromatic amino-acids and related peptides. I. Tyrosine. J Am Chem Soc 97:2599–2606.

Brahma A, Mandal C, Bhattacharyya D. 2005. Characterization of a dimeric unfolding intermediate of bovine serum albumin under mildly acidic condition. Biochim Biophys Acta 1751(2):159–169.

Brewer SH, Glomm WR, Johnson MC, Kang MK, Franzen S. 2005. Probing BSA binding to citrate-coated gold nanoparticles and surfaces. Langumuir 21:9303–9307.

Brown KR, Walter DG, Natan MJ. 2000. Seeding of colloidal Au nanoparticle solutions. 2. Improved control of particle size and shape. Chem Mater 12:306–313.

Cho SJ, Jarrett BR, Louie AY, Kauzlarich SM. 2006. Gold-coated iron nanoparticles: A novel magnetic resonance agent for T1 and T2 weighted imaging. Nanotechnology 17:640–644.

Chu M, Song X, Cheng D, Liu S, Zhu J. 2006. Preparation of quantum dot-coated magnetic polystyrene nanospheres for cancer cell labelling and separation. Nanotechnology 17:3268–3273.

Creed D. 1984a. The photophysics and photochemistry of the near-uv absorbing amino acids—iii. Cystine and its simple derivatives. Photochem Photobiol 39:577–583.

Creed D. 1984b. The photophysics and photochemistry of the near-uv absorbing amino acids—i. Tryptophan and its simple derivatives. Photochem Photobiol 39:537–562.

Creed D. 1984c. The photophysics and photochemistry of the near-uv absorbing amino-acids .ii. Tyrosine and its simple derivatives. Photochem Photobiol 39:563–575.

Creighton TE. 1993. Proteins: Structures & molecular properties. 2nd edition. New York: W H Freeman & Co; pp. 293–296.

Cushing BL, Kolesnichenko VL, O'Connor CJ. 2004. Recent advances in the liquid-phase syntheses of inorganic nanoparticles. Chem Rev 104:3893–3946.

Daniel MC, Astruc D. 2004. Gold nanoparticles: Assembly, supramolecular chemistry, quantum-size-related properties, and applications toward biology, catalysis, and nanotechnology. Chem Rev 104:293–346.

Di Felice R, Selloni A. 2004. Adsorption modes of cysteine on Au (111): Thiolate, amino-thiolate, disulfide. J Chem Phys 120:4906–4914.

Duroux M, Skovsen E, Petersen MTN, Duroux L, Gurevich L, Petersen SB. 2007. Light-induced immobilisation of biomolecules as an attractive alternative to microdroplet dispensing-based arraying technologies. Proteomics 7:3491–3499.

Gnanaprakash G, Philip J, Jayakumar T, Raj B. 2007. Effect of digestion time and alkali addition rate on physical properties of magnetite nanoparticles. J Phys Chem B 111:7978–7986.

Grossweiner LI, Usui Y. 1971. Flash photolysis and inactivation of aqueous lysozyme.

Haugland RP. 2002. Handbook of fluorecent probes and research products. 9th edition. USA: Molecular Probes, Inc.

Huang CY, Lee YD. 2006. Core–shell type of nanoparticles composed of poly[(n-butyl cyanoacrylate)-co-(2-octyl cyanoacrylate)] copolymers for drug delivery application: Synthesis, characterization and in vitro degradation. Int J Pharm 325:132–139.

Imahori H, Fukuzumi S, Porphyrin S. 2001. Porphyrin monolayer-modified gold clusters as photoactive materials. Adv Mater 13:1197–1199.

Ito A, Hayashida M, Honda H, Hata K, Kagami H, Ueda M, Kobayashi T. 2004. Construction and harvest of multilayered keratinocyte sheets using magnetite nanoparticles and magnetic force. Tissue Eng 10:873–880.

Jonkheijm P, Weinrich D, Schröder H, Niemeyer CM, Waldmann H. 2008. Chemical stratergies for generating protein biochips. Angew Chem Int Ed Engl 47:9618–9647.

Kerwin BA, Remmele RL, Jr. 2007. Protect from light: Photodegradation and protein biologics. J Pharm Sci 96:1468–1479.

Koneracka M, Kopcansky P, Timko M, Ramchand CN, de Sequeira A, Trevan M. 2002. Direct binding procedure of proteins and enzymes to fine magnetic particles. J Mol Catal B: Enzym 18:13–18.

Lattuada M, Hatton TA. 2007. Functionalization of monodisperse magnetic nanoparticles. Langmuir 23:2158–2168.

Laurent S, Forge D, Port M, Roch A, Robic C, Elst LV, Muller RN. 2008. Magnetic iron oxide nanoparticles: Synthesis, stabilization, vectorization, physicochemical characterizations, and biological applications. Chem Rev 108:2064–2110.

Lee SH, Liddell CM. 2009. Anisotropic magnetic colloids: A strategy to form complex structures using nonspherical building blocks. Small 5:1957–1962.

Lesnikovich AI, Shunkevich TM, Naumenko VN, Vorobyova SA, Baykov MV. 1990. Dispersity of magnetite in magnetic liquids and the interaction with a surfactant. J Magn Magn Mater 85:14–16.

Li Z, Lee WE, Galley WC. 1989. Distance dependence of the tryptophan–disulfide interaction at the triplet level from pulsed phosphorescence studies on a model system. Biophys J 56:361–367.

Li Y, Xu X, Deng C, Yang P, Zhang X. 2007. Immobilization of trypsin on superparamagnetic nanoparticles for rapid and effective proteolysis. J Proteome Res 6:3849–3855.

Lim JK, Kim Y, Lee SY, Joo SW. 2008. Spectroscopic analysis of l-histidine adsorbed on gold and silver nanoparticle surfaces investigated by surface-enhanced Raman scattering. Spectrochim Acta Part A 69: 286–289.

Lyon JL, Fleming DA, Stone MB, Schiffer P, Williams ME. 2004. Synthesis of Fe oxide core/Au shell nanoparticles by iterative hydroxylamine seeding. Nano Lett 4:719–723.

Ma Z, Guan Y, Liu H. 2006. Superparamagnetic silica nanoparticles with immobilized metal affinity ligands for protein adsorption. J Magn Magn Mater 301:469–477.

Mehta RV, Upadhyay RV, Charles SW, Ramchand CN. 1997. Direct binding of protein to magnetic particles. Biotechnol Tech 11:493–496.

Neves-Petersen MT, Duroux M, Skovsen E, Duroux L, Petersen SB. 2009a. Printing novel molecular architectures with micrometer resolution using light. J Nanosci Nanotechnol 6:3372–3381.

Neves-Petersen MT, Klitgaard S, Pascher T, Skoven E, Polivka T, Yartsev A, Sundstrom V, Petersen SB. 2009b Flash Photolysys of cutinase: Identification and decay kinetics of transient intermediates formed upon UV excitation of aromatic residues. Biophys J 97:211–226.

Park HY, Schadt MJ, Wang L, Lim IIS, Njoki PN, Kim SH, Jang MY, Luo J, Zhong CJ. 2007. Fabrication of magnetic core@shell Fe oxide@Au nanoparticles for interfacial bioactivity and bio-separation. Langmuir 23:9050–9056.

Petersen MTN, Snabe T, Klitgaard S, Duroux M, Petersen SB. 2006. Photonic activation of disulfide bridges achieves oriented protein immobilization on biosensor surfaces. Protein Sci 15:343–351 (Photochem Photobiol 13:195–214).

Riener CK, Kada G, Gruber HJ. 2002. Quick measurement of protein sulfhydryls with Ellman's reagent and with 4,4′-dithiodipyridine. Anal Bioanal Chem 373:266–276.

Safarik I, Safarikova M. 2002. Magnetic nanoparticles and biosciences. Munatsh Chem 133:737–759.

Sander MU, Luther K, Troe J. 1993. Excitation energy dependence of the photoionization of liquid water. J Phys Chem 97:11489–11492.

Schmid G, Corain B. 2003. Nanoparticulated gold: Syntheses, structures, electronics, and reactivities. Eur J Inorg Chem 17:3081–3098.

Schwertmann U, Cornell RM. 1991. Iron oxides in the laboratory. Weinheim: VCH Verlagsgesellschaft, p. 137.

Sharma P, Brown S, Walter G, Santra S, Moudgil B. 2006. Nanoparticles for bioimaging. Adv Colloid Interface Sci 123–126:471–485.

Skoven E, Kold A, Petersen MTN, Petersen SB. 2009a. Photonic immobilization of high density protein arrays using Fourier optics. Proteomics 9:3945–3948.

Skoven E, Petersen MTN, Laurent D, Kold A, Petersen SB. 2009b. Immobilizing biomolecules near the diffraction limit. J Nanosci Nanotech 9:4333–4337.

Templeton AC, Cliffel DE, Murray RW. 1999. Redox and fluorophore functionalization of water-soluble, tiopronin-protected gold clusters. J Am Chem Soc 121:7081–7089.

Tronc E, Belleville P, Jolivet J-P, Livage J. 1992. Transformation of ferric hydroxide into spinel by iron (II) adsorption. Langmuir 8: 313–319.

Ullman A. 1996. Formation and structure of self-assembled monolayers. Chem Rev 96:1533–1554.

Uvdal K, Bodo P, Liedberg B. 1992. L-Cysteine adsorbed on gold and copper: An X-ray photoelectron spectroscopy study. J Colloid Interface Sci 149:162–173.

Vanhooren A, De Vriendt K, Devreese B, Chedad A, Sterling A, Dael HV, Beeumen JV, Hanssens I. 2006. Selectivity of tryptophan residues in mediating photolysis of disulfide bridges in goat α-lactalbumin. Biochemistry 45:2085–2093.

Varghese N, Vivekchand SRC, Govindaraj A, Rao CNR. 2008. A calorimetric investigation of the assembly of gold nanorods to form necklaces. Chem Phys Lett 450:340–344.

Wang L, Luo J, Fan Q, Suzuki M, Suzuki IS, Engelhard MH, Lin Y, Kim N, Wang JQ, Zhong CJ. 2005. Monodispersed core–shell Fe_3O_4@Au nanoparticles. J Phys Chem B 109:21593–21601.

Wang X, Guo L, Ma H. 2009. Analysis of local polarity change around Cys34 in bovine serum albumin during N→B transition by a polarity-sensitive fluorescence probe. Spectrochim Acta Part A: Mol Biomol Spectrosc 73:875–878.

Yang H, Zhang S, Chen X, Zhuang Z, Xu J, Wang X. 2004. Magnetite-containing spherical silica nanoparticles for biocatalysis and bioseparations. Anal Chem 76:1316–1321.

Yang Z, Si S, Zhang C. 2008. Magnetic single-enzyme nanoparticles with activity and stability. Biochem Biophys Res Commun 367:169–175.

You CC, Miranda OR, Gider B, Ghosh PS, Kim IB, Erdogan B, Krovi SA, Bunz U, Rotello VM. 2007. Detection and identification of proteins using nanoparticle-fluorescent polymer 'chemical nose' sensors. Nat Nanotechnol 2:318–323.

You CC, Agasti SS, Rotello VM. 2008. Isomeric control of protein recognition with amino- and dipeptide-functionalized gold nanoparticles. Chem Eur J 14:143–150.

Zhu Y, Cheng G, Dong S. 2001. The electrochemically induced conformational transition of disulfides in bovine serum albumin studied by thin layer circular dichroism spectroelectrochemistry. Biophys Chem 90: 1–8.